Journal of Controlled Release 304 (2019) 7–18

Contents lists available at ScienceDirect

Journal of Controlled Release

journal homepage: www.elsevier.com/locate/jconrel

Gold nanocluster-loaded hybrid albumin nanoparticles with fluorescence-based optical visualization and photothermal conversion for tumor detection/ablation

Sanghyun Park[a], Hanju Kim[a], Su Chan Lim[a], Kyungseop Lim[a], Eun Seong Lee[b], Kyung Taek Oh[c], Han-Gon Choi[d], Yu Seok Youn[a,*]

[a] School of Pharmacy, Sungkyunkwan University, 2066 Seobu-ro, Jangan-gu, Gyeonggi-do, Suwon 16419, Republic of Korea
[b] Division of Biotechnology, The Catholic University of Korea, 43 Jibong-ro, Gyeonggi-do, Bucheon-si 14662, Republic of Korea
[c] College of Pharmacy, Chung-Ang University, 84 Heukseok-ro, Dongjak-gu, Seoul 06974, Republic of Korea
[d] College of Pharmacy, Hanyang University, 55 Hanyangdaehak-ro, Sangnok-gu, Ansan 15588, Republic of Korea

ARTICLE INFO

Keywords:
Gold nanoclusters
Albumin nanoparticles
Hyperthermia
LSPR
FRET
Antitumor therapy

ABSTRACT

Gold nanoclusters (AuNCs) are viewed as effective hyperthermal agents for the treatment of tumors. Whereas AuNCs formed by the agglomeration of several to tens of gold atoms (< 1–2 nm) possess significant fluorescence, they have a negligible hyperthermal effect, while AuNCs comprised of spherical gold nanoparticles (AuNPs > a few nanometers) have a marked hyperthermic effect but lose their inherent fluorescence and obstruct the intensity of neighboring fluorescent dyes due to Forster resonance energy transfer (FRET). To achieve both hyperthermia and fluorescence-based optical visualization, we generated hybrid albumin nanoparticles containing AuNCs (~88 nm) comprising AuNPs (~4.5 nm). We generated a series of formulated AuNCs and optimized the size, morphology, NIR absorbance (600–900 nm), hyperthermal activity, and fluorescence spectral characters of the resulting hybrid albumin nanoparticles (AuNCs/BSA-NPs) by considering the interparticle distance between the AuNPs and Cy5.5. Among these, AuNCs/BSA-NPs (formula D) had a strong hyperthermic effect and had well-preserved fluorescence intensity (from the attached Cy5.5) due to localized surface plasmon resonance (LSPR) and a reduction in FRET. These AuNCs/BSA-NPs were able to elevate the surface tumor temperature of HCT116-bearing mice to > 50 °C following 808 nm laser irradiation (1.5 W/cm^2, 10 min), which remarkably suppressed tumor growth (17.8 ± 16.9 mm^3 *vs.* PBS and AuNCs/BSA-NPs (formula E): ~1850 and ~1250 mm^3, respectively). Also, Cy5.5-modified AuNCs/BSA-NPs (formula D) showed good performance in optical fluorescence imaging of target tumors in HCT116 tumor-bearing mice. Together, our results indicate that the interparticle distance between albumin or Cy5.5 and AuNPs/AuNCs can be optimized to achieve both hyperthermia and fluorescence emission by striking a balance between LSPR and FRET effects. We believe that the AuNC/BSA-NPs formulation presented here can serve as a potential platform for both optically visualizing and treating colon cancers.

1. Introduction

Photothermal therapy (PTT) is an attractive way to treat solid tumors because of its noticeable tumor ablation effect with minimum impact on normal tissues [1,2]. Among several methods to elevate the local temperature of tumors (*e.g.*, ultrasound, radiofrequency, or microwaves) [3–5], gold nano-platforms such as spheres, rods, shells, and clusters have gained interest as promising agents for PTT [6,7]. Gold nanospheres and nanorods show remarkable performance because they emit heat responding to near-infrared (NIR) laser light based on the phenomenon of localized surface plasmon resonance (LSPR) [7,8]. Furthermore, the hyperthermia of gold nanoparticles stimulated with NIR laser light can be finely controlled by a few factors (irradiation time, laser intensity, and gold concentration) for specific purposes in anticancer therapy [9]. Mild and moderate hyperthermia (~43 °C) boosters the antitumor effects of chemotherapy and radiotherapy in a synergistic manner due to enhanced drug permeation and blood flow [6,10–12], whereas severe hyperthermia (temperatures > 46 °C) causes cell death and tumor ablation over the long term [1,6,13].

Spherical gold nanoparticles (hereafter termed AuNPs) respond only

* Corresponding author.
E-mail address: ysyoun@skku.edu (Y.S. Youn).

https://doi.org/10.1016/j.jconrel.2019.04.036
Received 19 December 2018; Received in revised form 2 April 2019; Accepted 23 April 2019
Available online 24 April 2019

to visible light in the wavelength range from 500–580 nm, which barely penetrates deep tissues due to interference by hemoglobins, skin, and other tissue components [6,7]. The peak absorptions for 10 nm and 100 nm AuNPs are at 520 and 580 nm, respectively, which indicates that the NIR absorption of smaller AuNPs is seriously hampered [14]. Therefore, AuNPs are practically inadequate for photothermal therapy in the clinical field [15,16]. AuNPs larger than 6–8 nm barely pass through the glomerulus (basement membrane pores: ~6 nm), and the unfiltered fraction of AuNPs may cause long-term toxicity during systemic circulation on account of their non-degradability [17–21].

Unlike single AuNPs, nano-sized agglomerations of AuNPs (gold nanoclusters; AuNCs) possess strengthened NIR absorption over the wide wavelength range of 650 to 950 nm due to the so-called red-shift phenomenon [22,23]. Consequently, AuNCs display very high hyperthermal conversion efficiency *versus* AuNPs, enhancing tumor suppression. Unlike the high fluorescence of AuNCs comprised of several to tens of gold atoms (< 1–2 nm) [24,25], AuNCs comprised of AuNPs larger than a few nanometers tend to lose their inherent fluorescence [26]. This prevents use of the AuNCs to detect or diagnose target tumors *in vivo*. Furthermore, the intensity of fluorescent probes tagged to the AuNCs is quenched to an extent inversely proportional to the distance between probes and AuNCs due to Forster resonance energy transfer (FRET) [27,28]. This prevents fluorescence-based *in vivo* optical imaging to visualize the target tumor region; X-ray computed tomography (CT) and photoacoustic (PA) imaging need to be used instead [29–31].

Herein, we sought to design and fabricate AuNC-loaded hybrid albumin nanoparticles (AuNCs/BSA-NPs) for ablation and optical visualization of target tumors by emitting heat and fluorescence in response to NIR light, respectively. We have previously shown that albumin nanoparticles have good targeting ability and can be used to visualize and suppress solid tumors [32–34]. Here, we took advantage of the characteristics of albumin nanoparticles by using them as a second targeting carrier. Albumin quantity was considered to be a critical factor affecting the distances between respective AuNPs or AuNCs and Cy5.5 dye. To simultaneously maximize the hyperthermal effect and preserve fluorescence intensity, the formulae for hybrid gold-albumin nanoparticles were optimized by adjusting the quantities of AuNPs/AuNCs and albumin. Analytical/morphological investigations, *in vitro* cytotoxicity tests, and *in vivo* antitumor efficacy experiments were used to achieve this purpose (Fig. 1).

2. Materials and methods

2.1. Materials

Bovine serum albumin (BSA; 66.4 kDa and ~98%) was purchased from MP Biomedicals (Solon, OH, USA). Gold(III) chloride ($HAuCl_4$) and sodium citrate ($Na_3C_6H_5O_7$) were purchased from Sigma-Aldrich (St. Louis, MO, USA). Cy 5.5-NHS ester was purchased from GE Healthcare (Buckinghamshire, UK). Sodium borohydride ($NaBH_4$) was purchased from TCI (Toshima, Kita-ku, Tokyo, Japan). The HCT 116 (ATCC CCL-247™) human colorectal carcinoma cell line was obtained from the American Type Culture Collection (Rockville, MD, USA). DMEM and fetal bovine serum (FBS) were purchased from Capricorn (Ebsdorfergrund, Hesse, Germany). Trypsin-EDTA and penicillin-streptomycin (P/S) solution were purchased from Corning (Corning, NY, USA). The LIVE/DEAD® viability/cytotoxicity assay kit was purchased from Thermo Fisher Scientific (Rockford, IL, USA). All other reagents were obtained from Sigma-Aldrich unless otherwise indicated.

2.2. Animals

BALB/c *nu/nu* mice (male, 5 weeks old) were purchased from Raonbio Inc. (Yongin, South Korea). Animals were cared for in accordance with the guidelines issued by the National Institutes of Health (NIH) for the care and use of laboratory animals (NIH publication 80-23, revised in 1996). Animals were caged in groups of 5 under a 12-h light/dark cycle with food and water. Animals were acclimatized for 2 weeks. All animal experiments were conducted under guidelines approved by Sungkyunkwan University.

2.3. Synthesis of gold nanoparticles (AuNPs)

Gold nanoparticles (AuNPs) around 5 nm were manufactured by reduction of $HAuCl_4$ using sodium citrate and $NaBH_4$ as reducing agents ($Au^{3+} \rightarrow Au^0$) [35]. First, 1 mL of $HAuCl_4$ (1 wt% (*w/v*)) was added to 50 mL of deionized water (DW) and stirred at 600 rpm. Next, 2 mL of a sodium citrate solution (38.8 mM) was added to the mixture. After 2 min, 1 mL of 0.075% (w/v) $NaBH_4$ dissolved in 38.8 mM sodium citrate solution was added slowly in a dropwise manner for 5 min. The AuNP solution was further purified and centrifuged with a centrifugal filter (Amicon® 30 K ultra centrifugal filters) three times at 2000 rpm for 15 min at 4 °C and stored at 4 °C until required.

2.4. Preparation of gold nanoclusters (AuNCs) and AuNC-loaded BSA-nanoparticles (AuNCs/BSA-NPs)

AuNCs were prepared using previously described methods with slight modifications with the final goal of fabricating agglomerated AuNPs [36,37]. AuNP solution (6 mg/mL; 0.1 mL) was dropwise added to solutions with different concentrations of BSA (3 mL; 0.01, 0.1, 1, 10 and 100 mg/mL; 100 mM PB, pH 8.0) and then stirred at 200 rpm. The AuNCs so prepared and purified are referred to as formulae A, B, C, D, and E, respectively. AuNCs/BSA-NPs were fabricated by incorporating AuNCs into naïve or Cy5.5 (cyanine dye 5.5)-labeled-albumin nanoparticles (BSA-NPs) *via* a desolvation process [32,38]. Ethanol (1.2 mL) was added dropwise (1 mL/min) to mixed solutions of 0.1 mL AuNCs (0.6, 1.2, 2.4 and 4.8 mg/mL; 0.1 mM, pH 8.0 phosphate buffer) and 0.1 mL naïve BSA (40 mg/mL; DW) or Cy5.5-BSA (80 μg: 4 mg feed ratio; 40 mg/mL; DW). After desolvation, 1 μL of 50% glutaraldehyde was added to the resulting solutions immediately and albumin molecules were allowed to crosslink for 12 h under stirring at 200 rpm. Respective solutions were centrifuged at 3000 rpm for 10 min using Amicon® 30 K ultra-centrifugal filters to remove the supernatant that contained unreacted BSA/Cy5.5-BSA and unincorporated AuNCs. The spin-down fraction of AuNCs/BSA-NPs was resuspended with DW.

2.5. Characterization of AuNPs, AuNCs, and AuNCs/BSA-NPs

The sizes of AuNPs, AuNCs and AuNCs/BSA-NPs were measured by a particle size analyzer (Zetasizer Nano ZS90, Malvern Instruments, Worcestershire, UK) at a 90° degree scattering angle using dynamic light scattering. To analyze zeta potentials, samples were put in cuvettes (DTS1070 folded capillary cells) and analyzed with the same analyzer using laser Doppler microelectrophoresis. The morphology and microstructure of the nanoparticle solutions were analyzed by transmission electron microscopy (JEM-3010, JEOL Ltd., Tokyo, Japan). UV-Vis absorbance spectra were obtained with a Tecan Infinite M200 spectrophotometer (Tecan Group, Switzerland) in the wavelength region from 450 to 900 nm. Fluorescence intensity was measured with the same spectrophotometer at λ_{ex} = 670 nm, λ_{em} = 710 nm. Fluorescence spectra were measured at a fixed excitation wavelength of 640 nm and emission wavelength ranging from 670 to 850 nm (scan interval 10 nm) to identify the near-infra red fluorescence-emitting dye Cy5.5. Fluorescence images were obtained using an optical imaging system (Lago-X, Spectral Instruments Imaging, Inc., AZ, USA).

2.6. Quantitation of AuNPs, AuNCs, and AuNCs/BSA-NPs

The actual concentrations of AuNPs, AuNCs, and AuNCs/BSA-NPs were measured by inductively coupled plasma optical emission

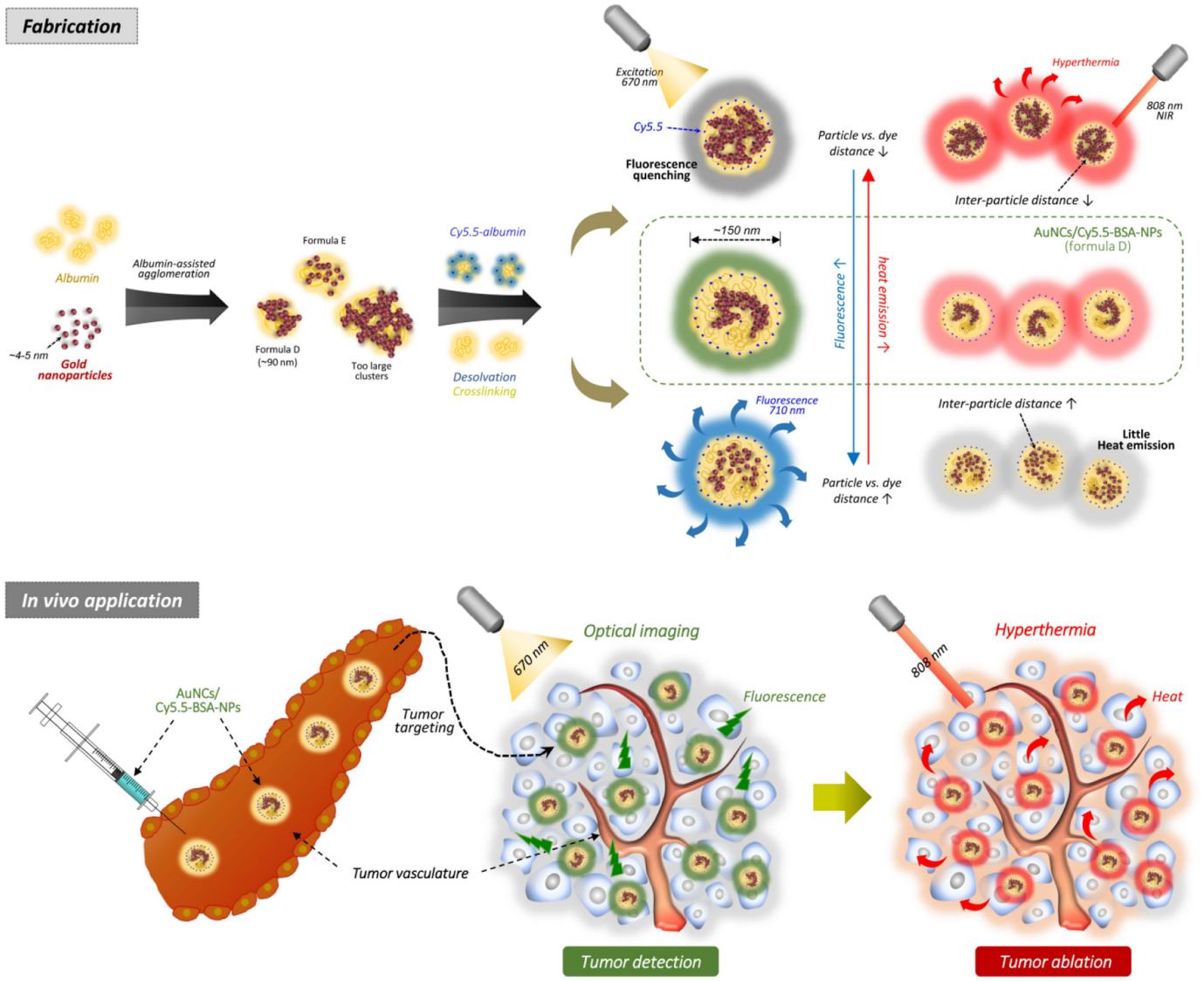

Fig. 1. Schematic illustration of the design, preparation, and *in vivo* application of gold nanocluster-loaded Cy5.5-albumin nanoparticles (AuNCs/Cy5.5-BSA-NPs) with fluorescence intensity and hyperthermal activity for tumor detection/ablation. (For interpretation of the references to colour in this figure legend, the reader is referred to the web version of this article.)

spectrometry (ICP-OES, Varian 720-ES, Agilent Technologies Inc., USA). A 4.0 mL portion of aqua regia, which is a mixture of nitric acid (HNO_3) and hydrochloric acid (HCl) at a 1:3 molar ratio, was added to the nanoparticle solutions. The samples were put in a graphite block acid digestion system at 200 °C. After 4 h, samples were cooled down and analyzed by ICP-OES. These experimental processes were carried out in a cooperative center for research facilities at Sungkyunkwan University.

2.7. *In vitro and in vivo photothermal conversion*

For *in vitro* studies, AuNCs and AuNCs/BSA-NPs with 200 μg/mL Au were prepared and irradiated by 808 nm NIR laser (1.5 W/cm^2) for 10 min. Hyperthermal effects due to the photothermal conversion of AuNCs and AuNCs/BSA-NPs were assessed by thermographic camera (FLIR E85 24°, FLIR systems, Inc., Wilsonville, USA). For *in vivo* studies, a 200 μL portion of AuNCs/BSA-NPs (10 mg/mL) was injected into HCT 116 tumor-bearing mice through the tail vein. After 6 h, an 808 nm NIR laser (1.5 W/cm^2) was used to irradiate the tumor site for 10 min. Temperature-based thermal images were visualized using a thermographic camera.

2.8. *Visualization of the uptake of AuNCs/BSA-NPs by HCT 116 cells using CLSM and Bio-TEM*

Cellular uptake of AuNCs/BSA-NPs into HCT 116 cells was visualized by confocal laser scanning microscopy (CLSM; LSM510, Carl Zeiss Meditec AG, Jena, Germany). First, 150 μL of HCT 116 cells (1.5×10^5 cells/mL) in DMEM (10% FBS, 1% P/S) were seeded into removable 12-well silicon chambers (Ibidi, Martinsried, Germany) and incubated for 24 h. Prior to the experiment of nanoparticle internalization, cell media was replaced with DMEM (1% FBS, 1% P/S) to slow down the rate of cell growth and provide the stable cell state. Cy5.5-AuNCs/BSA-NPs (formula D; 75 and 300 μg/mL as Au) and Cy5.5-AuNCs/BSA-NPs (formula E; 75 μg/mL as Au) were added to wells to compare fluorescence intensity or quenching. At predetermined times (3, 6, 12, and 24 h), the cells were washed twice with DMEM (1% FBS, 1% P/S) and observed by CLSM to detect Cy5.5 fluorescence. To confirm the cellular uptake of AuNCs/BSA-NPs, HCT 116 cells were seeded in cell culture flasks and treated with AuNCs/BSA-NPs (formula D; 20 μg/mL). After 24 h, cells were detached using trypsin and centrifuged three times at 900 rpm for 5 min with PBS and fixed by adding 1 mL of 2.5% glutaraldehyde in 0.1 M phosphate buffer (pH 7.4). The remaining steps after

fixation were performed at the Korea Basic Science Institute (Cheongju, Korea). Fixed cells were observed by bio-transmission electron microscopy (TEM) (Tecnai G^2 spirit twin, FEI company, Hillsboro, OR, USA).

2.9. Cytotoxicity induced by NIR light irradiation of AuNCs/BSA-NPs in HCT 116 cells

Cytotoxicity was determined by utilizing the MTT assay and a live/dead assay kit. For MTT assay, 100 μL of HCT 116 cells (1.5×10^5 cells per mL) were added to wells of a 96-well cell culture plate (SPL, Korea) followed by a 1-day incubation. AuNCs/BSA-NPs (formulae D and E; 0, 10, 20, 50, 100 μg/mL as Au) were treated with DMEM media containing 1% FBS and 1% P/S. To compare photothermal effects, cells were treated with both formulae D and E NPs. After 1 day, cells were washed and irradiated with an 808 nm NIR laser at 1.5 W/cm^2 (Laserlab, Seoul, Korea) for 10 min. After 24 h, MTT solution (0.5 mg/mL) was added to each well and 100 μL dimethyl sulfoxide (DMSO) was then added to each well following removal of the remaining solution. Finally, absorbance intensity was measured by spectrometry at 562 nm (VersaMax microplate reader, Molecular Devices, CA, USA).

For the live/dead assay, HCT 116 cells were cultured as 2D monolayers and 3D spheroids. To create 2D monolayers, 100 μL aliquots of HCT 116 cells (2.0×10^5 cells per mL) were added to wells of a 12-well chamber (Ibidi, Martinsried, Germany), while for spheroids, HCT 116 cells (300 cells/well) were seeded in cell plates designed to induce the formation of 3D multicellular spheroids (Corning, NY, USA). The overall processes up to irradiation was the same as those described for the MTT assay. After 24 h, 100 μL of the live/dead working solution was added to each well. EthD-1 and calcein-AM were used to stain dead cells as red and live cells as green, respectively. After 40 min, stained live or dead cells were detected by CLSM.

2.10. In vivo imaging of AuNCs/BSA-NPs

Cy5.5-modified AuNCs/BSA-NPs (formulae D and E; 0.4 mg/kg) and free Cy5.5 were injected *via* the tail veins of tumor-bearing mice to examine their tissue distribution and tumor targeting abilities. Cy5.5-intensity was adjusted to be equal in all groups, and fluorescence was visualized at 2, 4, 8, 24, 48, and 72 h using an *in vivo* imaging system (IVIS® Spectrum, PerkinElmer, USA) at the Korea Basic Science Institute (Cheongju, Korea). Separately, the accumulation of AuNCs/BSA-NPs (formula D and E) at tumor sites was visualized by photoacoustic (PA) imaging. When the volume of the tumor reached around 200 mm^3, 200 μL of PBS and AuNCs/BSA-NPs (formulae D and E; 10 mg/mL) were injected *via* the tail vein. At predetermined times (2, 4, 8, 24, and 72 h) post-injection, gold from each nanoparticle group was detected by a Vevo 3100 LAZR-X imaging system (FUJIFILM VisualSonics Inc. New York, USA) equipped with a 40 MHz, 256-element linear array detector.

2.11. In vivo antitumor efficacy of AuNCs/BSA-NPs

The *in vivo* antitumor efficacy of AuNCs/BSA-NPs (formulae D and E) was assessed in HCT 116 tumor-bearing mice. Aliquots (1×10^7) of HCT 116 cells in 100 μL of DMEM (10% FBS and 1% P/S) were subcutaneously injected in the right flank region of BALB/c *nu/nu* mice. When tumor volumes reached around 150 mm^3, HCT 116 tumor-bearing mice were divided into four groups: PBS without laser, AuNCs/BSA-NPs (formula D) with/without laser, and AuNCs/BSA-NPs (formula E) with laser. On day 0, 200 μL of PBS and AuNCs/BSA-NPs (10 mg/mL) were injected *via* tail vein. At 6 h after the injection, groups of mice were irradiated with an 808 nm NIR laser (1.5 W/cm^2) for 10 min. Tumor volume and body weight of the mice were measured every day. Tumor volume was measured with a caliper and calculated as $V = (L \times W^2)/2$, where V is tumor volume, L is tumor length, and W is tumor width. On day 20, mice were sacrificed, and their tumors were resected.

2.12. Histopathology of tumors and organs

Histopathology observation was performed for tumor tissue and major organs (liver, kidney, heart, lung, and spleen). Tumors were excised on day 1 after irradiation, and other organs were obtained at day 20. Each organ and tumor were treated with formalin solution. Hematoxylin and eosin (H&E) staining and *in vivo* TUNEL analysis were carried out by Logone Bio (Seoul, Korea).

2.13. Data analysis

Data are presented as means ± standard deviations (SD). The significance of differences was determined by Student's *t*-test. *P*-values < 0.05 were considered statistically significant.

3. Results and discussion

3.1. Fabrication of gold nanoclusters (AuNCs)

The primary goal of this study was to generate AuNCs with high photothermal activity and an appropriate size for incorporation into albumin nanoparticles (100–150 nm). AuNPs as the unit material for making AuNCs were synthesized to be < 5 nm because small nanoparticles are more easily filtered through the kidney and less toxic than large nanoparticles [19,39]. The *in vivo* biocompatibility of small gold nanoparticles is superior to that of large ones [40]. However, clusters of several to tens of gold atoms (< 1 nm) are documented to have negligible photothermal activity due to little NIR absorption [24]. Therefore, we fabricated AuNCs by agglomerating AuNPs with an average size of 4.4 ± 1.3 nm (Supporting Information Fig. S1a) by dropwise mixing of albumin solution. Agglomeration is attributable to albumin adsorption onto the AuNP surface followed by AuNP association [36,37,40]. The term of gold nanoclusters has been used for the nanostructure (< 1–2 nm) formed by agglomerating several to tens of gold atoms [24,25], rather than the bigger nanostructure (nano-aggregates or nano-agglomerates) that consisted of small AuNPs (> a few nanometers). However, AuNCs was used herein to refer to the latter as published previously [17,18]. In general, protein adsorption occurs due to electrostatic or hydrophobic interactions or a combination of both, and AuNP-protein agglomeration can be controlled by coating the molecules and controlling their density [36,37,40]. In our study, the quantity of albumin used had a large influence on the morphological and spectral characteristics of the AuNCs that formed. As shown in Fig. 2A, increasing the quantity of albumin (0.01–100 mg/mL: formulae A–E) reduced the particle size of AuNCs. Formula A resulted in large nano-aggregates (~882.1 nm) with an irregular morphology, while formulae D and E yielded smaller nano-aggregates (~87.9 and ~33.8 nm, respectively) due to the high amount of BSA they contained. We therefore considered these latter two formulae to be appropriate for albumin nanoparticle encapsulation (Supporting Information Fig. S1b–f). The quantity of BSA also affected the density of nanoclusters in terms of the interparticle distance of respective AuNPs; AuNCs made with formulae A or B were very dense and overlapped, while formula E yielded loosely clustered AuNCs (dispersed). In contrast, AuNCs made with formula D (10 mg/mL BSA) displayed a typical cluster morphology with moderate interparticle density. AuNCs made with formulae A- C were unstable and precipitated within 1 day, whereas those made with formulae D and E were stable for > 1 day without significant precipitation (Fig. 2B). Subsequently, AuNCs made using formula D or E were used in further experiments.

3.2. Preparation of AuNC-loaded BSA-NPs (AuNCs/BSA-NPs)

The next step was to prepare optimized AuNC-loaded BSA-NPs (either naïve or Cy5.5-tagged) with high photothermal activity and well-preserved fluorescence. Despite albumin coating of the AuNC surface,

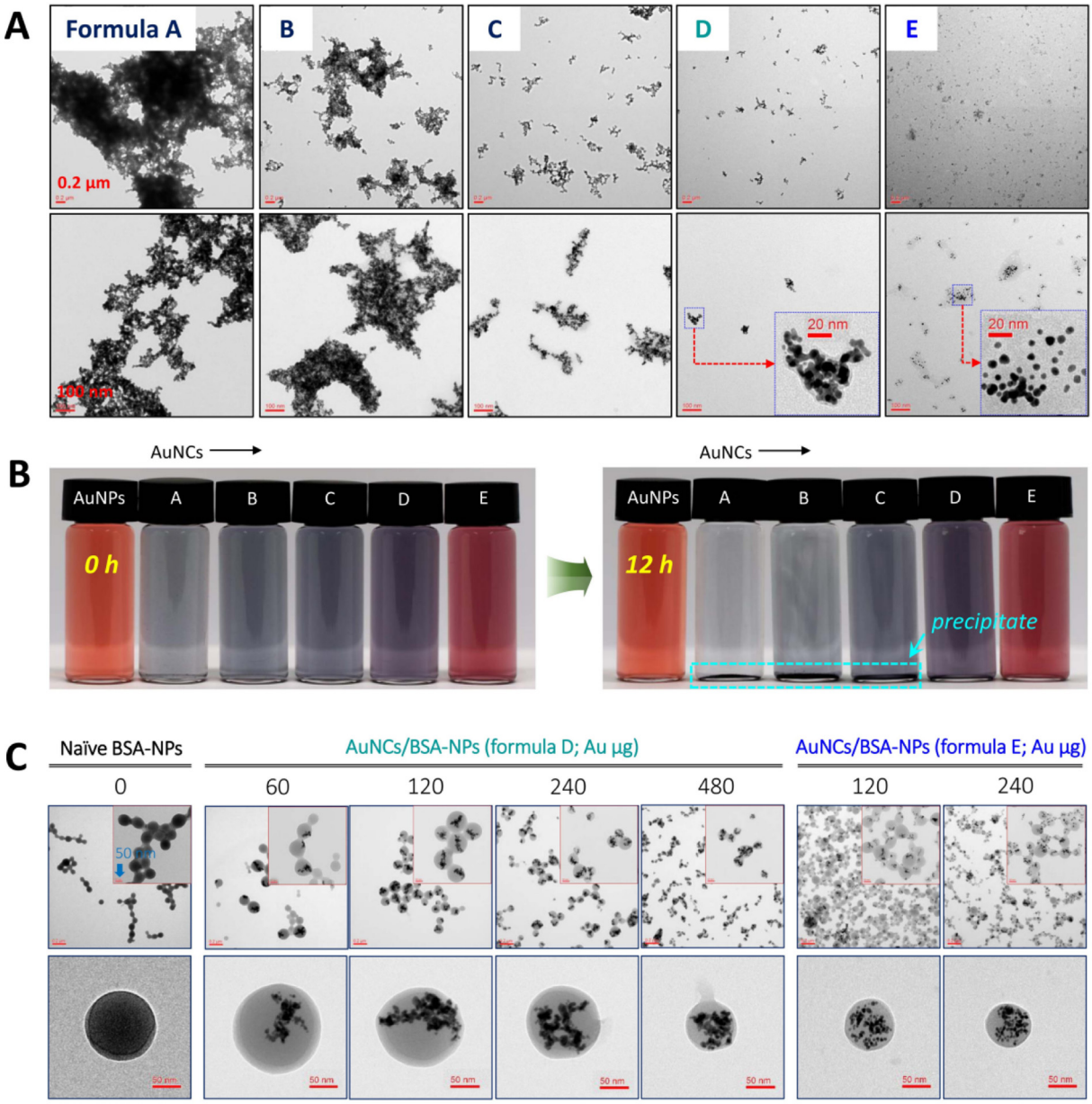

Fig. 2. (A) TEM images of gold nanoclusters (AuNCs) with different BSA concentrations (0.01, 0.1, 1, 10, 100 mg/mL; formulae A, B, C, D, and E, respectively) (magnification × 10,000 (upper) and × 20,000 (lower). Insets – enlarged AuNCs made with formulae D and E. (B) Photographs of AuNC solutions prepared with different BSA concentrations (0.01, 0.1, 1, 10, 100 mg/mL; formulae A, B, C, D, and E, respectively) to show their physical stability. (C) TEM images (upper) of naïve BSA nanoparticles (left); AuNC-loaded BSA nanoparticles (AuNCs/BSA-NPs; formula D) containing different Au amounts (60–480 μg) (middle); and AuNCs/BSA-NPs (formula E) containing different Au amounts (120 and 240 μg) (right). Insets show enlarged BSA-NPs and AuNCs/BSA-NPs (formulae D, E). Focused TEM images (lower) of single BSA-NPs and AuNCs/BSA-NPs (formulae D, E). (For interpretation of the references to colour in this figure legend, the reader is referred to the web version of this article.)

the therapeutic use of AuNCs alone is considered to be clinically inadequate in terms of tissue accumulation or toxicity. For this reason, we introduced a second targeting nano-carrier, albumin nanoparticles, which are able to completely encapsulate AuNCs. Nanoparticles made of proteins have attracted great attention because of their many pharmaceutical and clinical advantages as drug carriers for therapy or diagnosis of cancer [41–43]. Among these proteins, albumin is viewed as the most well-tolerated natural protein material with excellent biocompatibility and biodegradability and no critical toxicity to humans [32,44,45]. Moreover, albumin is able to effectively traverse the relatively leaky blood vessels and reach the tumor interstitium in two different ways: (i) gp60 (60 kDa glycoprotein as an albumin receptor present in endothelial cells)-mediated transcytosis and (ii) passive extravasation [46]. Overexpressed SPARC (Secreted Protein, Acidic and Rich in Cysteine) in the tumor extracellular matrix causes albumin/albumin nanoparticles to accumulate in tumor cells [47,48]. Furthermore, albumin has many functional groups, such as amines and carboxylates, that enable attachment of ligands or probes [49,50].

The albumin-based nanoparticle formulation of paclitaxel (Abraxane®; Celgene Corporation) has shown great success, and many unique methods to prepare albumin nanoparticle formulations, such as desolvation, emulsification, thermal gelation, nano-spray drying, and self-assembly have been developed [32,33,46,51–53]. We chose to use a desolvation process because it is one of the most well-established methods to form albumin coacervates and makes compact structure by crosslinking, resulting in tight entrapment of AuNCs [54]. However, a

negligible amount of AuNCs made with formulae A-C were incorporated into albumin nanoparticles (BSA-NPs) due to their large particle size (882–150 nm), and thus the formation of BSA-NPs was minimal when these formulae were used (Fig. 2C). Compared with naïve BSA-NPs (126.9 ± 32.5 nm), increased loading (or incorporation) of AuNCs (formulae D and E) resulted in a decrease in average particle size of AuNCs/BSA-NPs based on light scattering measurements (181.8 ± 50.5, 152.0 ± 52.6, 133.1 ± 52.2, 105.7 ± 44.0 nm for formula D and 110.2 ± 41.4, and 85.9 ± 33.2 nm for formula E). The smaller sizes of AuNCs/BSA-NPs generated using formula E is due to the smaller size of the AuNCs incorporated *versus* those incorporated using formula D (Supporting Information Fig. S2). Despite the change in particle size with different formulae, the incorporated AuNCs maintained their original morphology. The zeta potentials of AuNCs and AuNCs/BSA-NPs were all highly negative (−40 to −58 mV) and more negative than naïve BSA-NPs due to the incorporation of negatively charged AuNP components (Supporting Information Fig. S3).

3.3. Spectral characterization of AuNCs and AuNCs/BSA-NPs

The so-called 'water window' where aqueous tissue absorbs relatively little light in the wavelength range of 700–1200 nm [7,55], and especially the NIR region (wavelength from 650 to 950 nm), is the first therapeutic (biological) window that enables photothermal effects without harm to other tissues or cells [56,57].

Unlike individual AuNPs, AuNCs have been well documented to show LSPR in response to long wavelengths (*e.g.*, NIR > 800 nm), enabling deeper penetration into tissues and subsequent hyperthermia [6,7]. Plasmon oscillations of closely agglomerated AuNPs are likely to be coupled and lead to a strong red-shift of the LSPR wavelength because the near-field of AuNPs effectively interacts with neighboring particles [58,59]. Furthermore, the decreased interparticle distances in nanoclusters facilitates strong red-shift of the plasmon resonance, resulting in hyperthermia [60,61]. The UV-VIS-NIR spectra of AuNCs prepared using different amounts of BSA (formulae A-E) were completely different from those of AuNPs, which showed peak absorption at 520 nm (Fig. 3A). All AuNC formulations except AuNC-E exhibited remarkably greater absorbance over the wavelength range of 600–900 nm. This was due to the short interparticle distance between AuNPs, which was determined by the amount of BSA used in synthesis. Although AuNCs-A/B formulations displayed greatest NIR absorption than the other formulations due to tight agglomeration, they were not used on account of their large size and negligible incorporation in albumin nanoparticles. AuNCs-D also had high NIR absorption at 808 nm, but the spectrum of AuNCs-E showed marginally increased absorption *versus* AuNPs, with negligible absorption at ~808 nm. Subsequently, the peak ratios (%; 808 nm/520 nm) of AuNPs and AuNCs (formulae A~E) were 5.7, 116.3, 109.2, 100.9, 84.5, and 22.0%, respectively.

UV-VIS-NIR spectra of AuNCs/BSA-NPs (formulae D and E) were similar to those of their parents AuNCs. AuNCs/BSA-NPs(D) showed strong absorption at 808 nm but AuNCs/BSA-NPs(E) did not due to the relatively large spacing between AuNPs (Fig. 3A and B). In contrast, AuNCs/Cy5.5-BSA-NPs(E) exhibited well-preserved fluorescence around 700 nm corresponding to the maximum λ_{em} of Cy5.5 (Fig. 3C and D). However, an increase in incorporated AuNCs in BSA-NPs resulted in significantly reduced fluorescence intensity of AuNCs/Cy5.5-BSA-NPs(D) because surface Cy5.5 was quenched by the denser AuNCs-D (high amount) and the distance between Cy5.5 and AuNCs was obviously reduced based on observation of FRET. Consequently, AuNCs/Cy5.5-BSA-NPs(D) with 480 μg Au hardly emitted any fluorescence. In contrast, AuNCs/Cy5.5-BSA-NPs(D) with 60–120 μg Au were shown to have significant fluorescence, which enabled *in vivo* optical imaging (Fig. 3C and D).

3.4. Photothermal conversion and fluorescence emission of AuNCs/BSA-NPs and AuNCs/Cy5.5-BSA-NPs

The next important step was to evaluate the photothermal and fluorescence activities of the relevant hybrid gold-albumin nanoparticles (naïve or Cy5.5-tagged). The photothermal conversion of AuNCs and AuNCs/BSA-NPs (formulae D and E) was verified by thermographic camera *in vitro*. Formulae D and E (both AuNCs and AuNCs/BSA-NPs) were prepared at 200 μg/mL (as Au) and irradiated with an 808 nm NIR laser. Laser irradiation results in electron oscillations and transfer of energy to the environment by interfacial thermal conductance [62]. The surface temperature of AuNCs(D) and AuNCs/BSA-NPs(D) increased gradually up to ~70 °C for 10 min, whereas the surface temperature of AuNCs(E), AuNCs/BSA-NPs(E), and AuNPs was at most 40 °C (Fig. 4A and B). These results are attributable to the degree of red-shift caused by the LSPR in response to 808 nm irradiation: high absorption for formula D and low for formula E (Fig. 3B). We attributed the red-shift phenomenon of the LSPR observed for AuNCs made using formulae D and E to the distance between component AuNPs or BSA-NPs, which are responsible for conversion of light energy to heat energy.

To verify the hyperthermal effects of AuNCs/BSA-NPs (formulae D and E) *in vivo*, each formulation was injected into the tail vein of HCT116 tumor-bearing mice, and after 6 h, tumors were irradiated with an 808 nm laser. AuNCs/BSA-NPs accumulated in the tumors of each mouse (Fig. 4D). When visualized with a thermal imaging camera, the local tumor temperatures of mice injected with AuNCs/BSA-NPs(D) increased to > 50 °C at 5 min after NIR irradiation at 808 nm, which is sufficient for hyperthermia-based necrotic or apoptotic tumor cell death. In contrast, tumor temperature increased minimally when AuNCs/BSA-NPs(E) were irradiated at 808 nm (< 6 °C increase in temperature) (Fig. 4C). This finding demonstrates the targeting efficiency of albumin and the high photothermal efficiency of AuNCs/BSA-NPs(D).

Gold metal is a powerful fluorescence quencher that is 10 times stronger than typical dye-quenchers [63]. Therefore, fluorescent molecules located close to the AuNP surface have significantly decreased resonant energy transfer rates and radiative lifetimes [64]. In our study, Cy 5.5-labeled albumin was used to either coat AuNCs or incorporate AuNCs/BSA-NPs *via* modification of a desolvation method [34]. To preserve the surface fluorescence of AuNCs/Cy5.5-BSA-NPs, our strategy was to ameliorate the quenching effect of the AuNPs by providing an appropriate distance between AuNCs and Cy5.5 [32,65]. As shown in Fig. 4E, hyperthermia induced by Cy5.5-AuNCs (Cy5.5-BSA coated onto the surface of AuNCs) and AuNCs/Cy5.5-BSA-NPs(D) (Cy5.5-BSA as one of building materials for BSA-NPs) was similar but much higher than that of AuNCs/Cy5.5-BSA-NPs(E). Despite the high quantity of surface Cy5.5, the fluorescence intensity of AuNCs/Cy5.5-BSA-NPs(D) was weaker than that of AuNCs/Cy5.5-BSA-NPs(E) in terms of optically visualizing the surroundings. Again, these findings indicate that the interparticle distance between respective AuNPs comprising the AuNCs (either alone or with BSA-NPs incorporated) plays a critical role in heat emission based on red-shift of the LSPR. A close distance between Cy5.5 and AuNCs, which absorb excitation light, would seriously restricts fluorescence emission (λ_{ex} = 670 nm; λ_{em} = 710 nm) on account of the FRET phenomenon [27,28] and Purcell effect [66,67]. Despite the reduced fluorescence of AuNCs/Cy5.5-BSA-NPs(D), they exhibited much higher fluorescence than Cy5.5-BSA-AuNCs (almost nothing), and are therefore suitable for *in vivo* optical imaging.

3.5. Cellular uptake and fluorescence emission of AuNCs/BSA-NPs and AuNCs/Cy5.5-BSA-NPs in HCT116 cells

Cellular uptake of AuNCs/BSA-NPs and AuNCs/Cy5.5-BSA-NPs was visualized by using Bio-TEM and CLSM. As shown in Fig. 5A, HCT116 cells treated with AuNCs/Cy5.5-BSA-NPs(D) and (E) exhibited strong

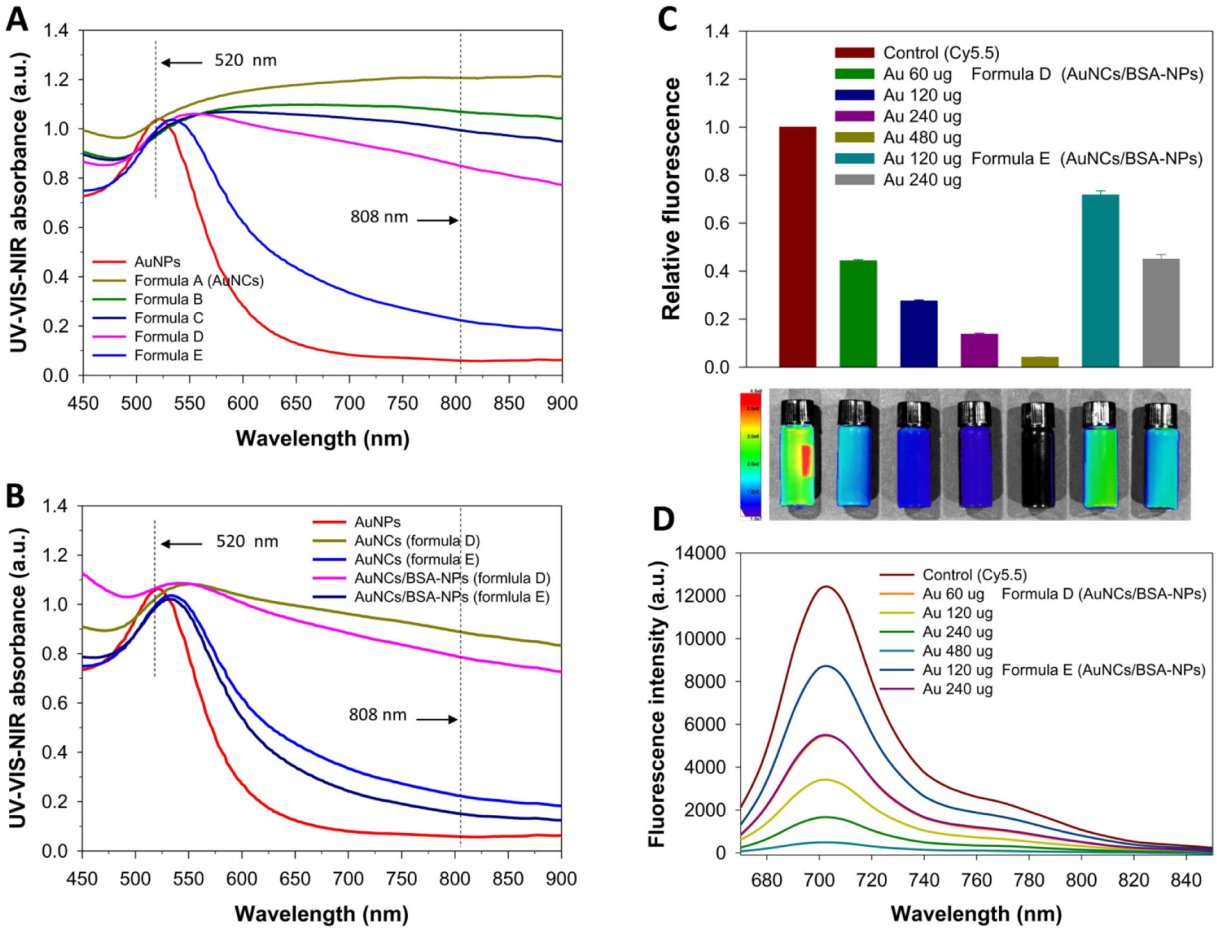

Fig. 3. (A) UV-Vis-NIR absorbance spectra of AuNPs and AuNCs (formulae A~E). (B) UV-Vis-NIR absorbance spectra of AuNPs, AuNCs (formulae D, E), and AuNCs/BSA-NPs (formulae D, E). (C) Relative fluorescence intensity (upper) of AuNCs (formulae D, E) for different Au amounts (60–240 μg) *vs.* intact Cy5.5 dye and optical visualization (lower). (D) Fluorescence spectra of intact Cy5.5 dye and AuNCs/BSA-NPs (formulae D, E) with different Au amounts (60–240 μg) at the excitation wavelength of 640 nm and emission wavelengths from 670 to 850 nm.

fluorescence, but the higher quantity of AuNCs(D) incorporated into BSA-NPs (120 *vs.* 480 μg), which translates to a shorter distance between Cy5.5 and AuNCs(D), quenched the fluorescence intensity inside HCT116 cells after internalization. To confirm internalization of AuNCs/BSA-NPs or AuNCs/BSA-NPs in HCT 116 cells, cells were photographed by bioTEM (Fig. 5B left). The diameter of HCT cells was estimated to be 10 μm, and AuNCs/BSA-NPs were present in nanoparticle vesicles in addition to being scattered around the cytosol, similar to what was observed for native AuNCs/BSA-NPs (Fig. 2C). AuNCs/BSA-NPs maintained their inherent shape and size and had photothermal activity. In contrast, AuNCs not incorporated into BSA-NPs were found to be less compact and exist individually without any signs of incorporation in nanoparticle vesicles (Fig. 5B right). These findings indicate that AuNCs/BSA-NPs can be internalized into HCT116 cells without surface ligands. The presence of vesicles and the nanoparticle size of AuNCs/BSA-NPs suggest endocytosis *via* clathrin-mediated endocytosis as the mechanism of internalization [68].

3.6. Cytotoxicity of AuNCs/BSA-NPs towards HCT116 cells

The cytotoxicity of AuNCs/BSA-NPs towards HCT 116 cells was evaluated through MTT and live/dead assays (Fig. 5C). HCT 116 cells were treated with different concentrations of AuNCs/BSA-NPs (formulae D and E; 0–100 μg/mL as Au) and 808 nm laser irradiation (10 min). The cytotoxicity of AuNCs/BSA-NPs(D) was 11.4-fold higher than that of AuNCs/BSA-NPs(E), with IC_{50} values of 27.3 and 310.2 μg/mL, respectively, due to the higher photothermal efficiency of the former than the latter. AuNCs/BSA-NPs(D) noticeably killed > 90% of HCT116 cells at the high concentration of 100 μg/mL.

In live/dead assays, both seeded 2D monolayers and 3D spheroids of HCT 116 cells were treated with PBS and AuNCs/BSA-NPs(D/E) with or without 808 nm laser irradiation. As shown in Fig. 5D, almost all cells were killed by AuNCs/BSA-NPs(D) (100 μg/mL) and 808 nm laser treatment, whereas approximately 50% were killed by the same procedure when AuNCs/BSA-NPs(E) were used. In contrast, hardly any cells were killed in the absence of laser irradiation, as visualized by staining with Calcein-AM, which fluoresces green. The overall results were similar to those obtained using the MTT assay. Similar to the 2D cell live/dead assay, HCT116 cell spheroids were treated with PBS and AuNCs/BSA-NPs(D/E) with or without 808 nm laser irradiation. Spheroids are *in vitro* three-dimensional tumor cell systems that mimic actual tumor tissues *in vivo* [69]. As shown in Fig. 5E, AuNCs/BSA-NPs (D) effectively killed cells of spheroids that were 250–300 μm in size, as evidenced by the widespread red fluorescence of the spheroids, and penetrated deep into the spheroids (10–50 μm Z-track images from slices with a 10-μm step size), whereas only 50% of spheroids treated with AuNCs/BSA-NPs(E) displayed red fluorescence (Fig. 5F). These findings demonstrate that AuNCs/BSA-NPs(D) had much better hyperthermal conversion activity than AuNCs/BSA-NPs(E) in terms of their enhanced LSPR for the same amount of irradiation.

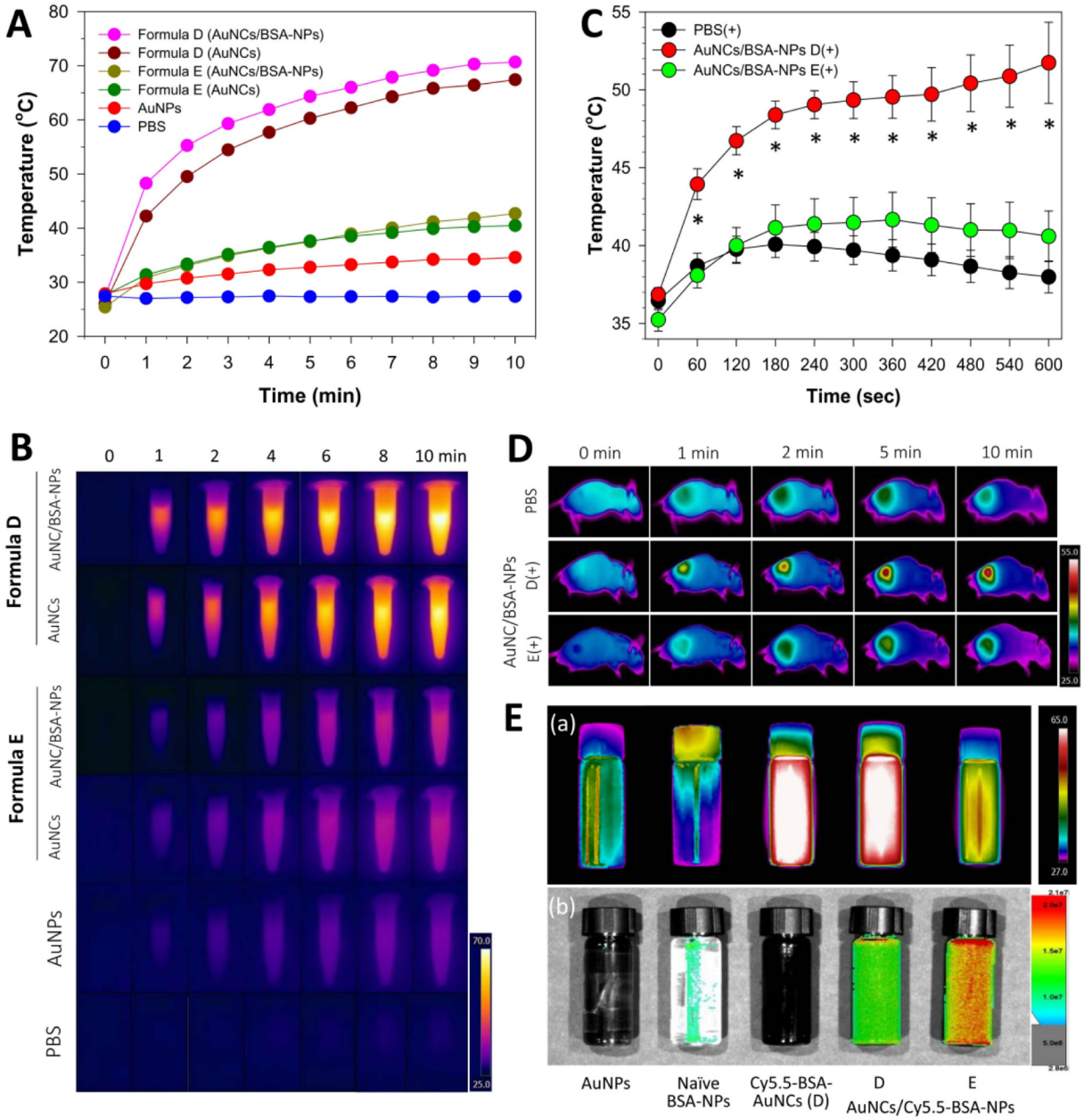

Fig. 4. (A) Temperature change profiles for photothermal conversion. PBS, AuNPs, AuNCs (formulae D, E), and AuNCs/BSA-NPs (formulae D, E) in Eppendorf tubes were irradiated with an 808 nm NIR laser (1.5 W/cm^2, 10 min) and (B) thermographic images were taken over 10 min. (C) Temperature change profiles of PBS and AuNCs/BSA-NPs (formula D, E) after 808 nm NIR laser irradiation (1.5 W/cm^2, 10 min) after injection *via* the tail vein into HCT116-bearing mice and (D) thermographic images taken over 10 min. (E) Thermographic and fluorescence optical images of AuNPs, BSA-NPs, Cy5.5-BSA-AuNCs (formula D), and AuNCs/Cy5.5-BSA-NPs (formulae D, E).

3.7. Photoacoustic and fluorescence imaging of AuNCs/BSA-NPs in HCT116 tumor-bearing mice

Tumor localization ability of AuNCs/BSA-NPs was investigated by photoacoustic (PA) imaging. PA imaging relies on signals of endogenous or exogenous contrast agents in tumor tissues, and gold is viewed as one of the most effective exogenous agents due to its strong SPR effect. The produced acoustic waves are converted into electric signal images [70,71]. The wavelength used for PA imaging is almost same as that used for photothermal therapy, which guarantees the usefulness of AuNCs/BSA-NPs [57,72]. As shown in Fig. 6A, unlike the tumor of a control mouse treated with PBS, the tumor of an AuNCs/BSA-NPs(D/E)-treated mouse showed strong resonance signal from the gold that accumulated in the tumor. Localized amounts of both AuNCs/BSA-NPs(D/E) were not significantly different until 72 h, with a maximum signal observed at 4–8 h.

The tumor targeting and tissue distributions of AuNCs/BSA-NPs(D/E) were identified by Cy5.5-based fluorescence optical imaging in HCT 116 tumor-bearing mice. Whereas free Cy5.5 dye injected *via* a tail vein was rapidly distributed throughout the body until 4 h and then rapidly eliminated from the blood circulation [73], AuNCs/BSA-NPs(D/E) accumulated gradually in the tumors until 72 h (Fig. 6B). Importantly, despite the lower fluorescence intensity of AuNCs/BSA-NPs(D) *in vitro* on account of partial FRET-based quenching, these nanoparticles allowed comparable or higher fluorescence visualization of relevant tumors than AuNCs/BSA-NPs(E). This finding indicates that AuNCs/BSA-NPs(D) have potential as an optical imaging agent to visualize or diagnose tumors. Aside from tumors, liver, spleen and kidney are

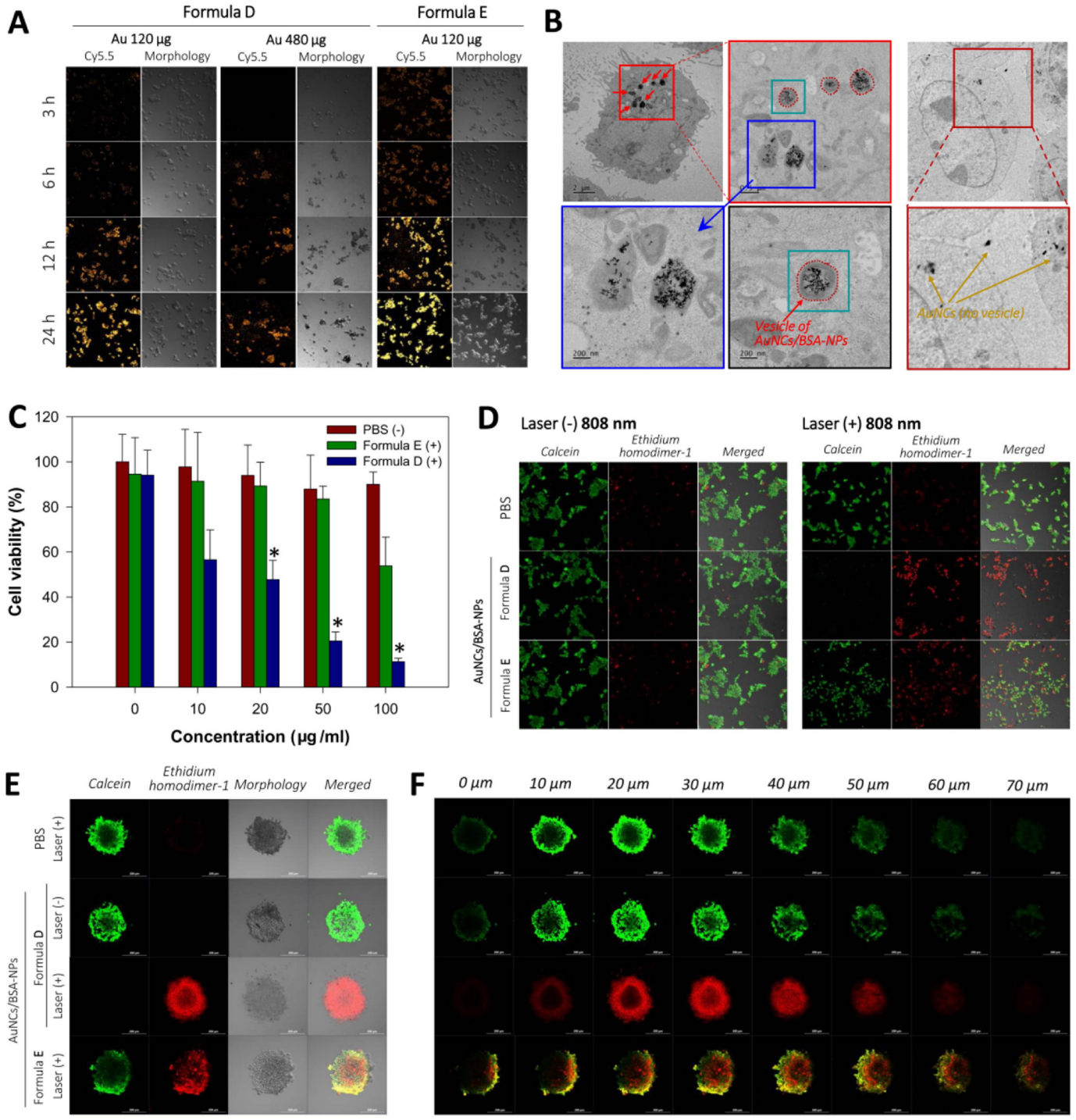

Fig. 5. (A) CLSM images of HCT116 cells after a 24 h-incubation with AuNCs/Cy5.5-BSA-NPs(D) (120 and 480 μg; left) or AuNCs/Cy5.5-BSA-NPs(E) (120 μg; right). (B) Bio-TEM images of AuNCs/BSA-NPs (left) and AuNCs alone (right) inside HCT 116 cells after internalization. (C) MTT assay-based cytotoxicity of PBS and AuNCs/BSA-NPs (formulae D, E) towards HCT 116 cells after irradiation with an 808 nm NIR laser (1.5 W/cm^2, 10 min). (D) Live/dead assay in 2D monolayer HCT 116 cells treated with PBS and AuNCs/BSA-NPs (formulae D, E) with (right) or without (left) 808 nm NIR laser irradiation (1.5 W/cm^2, 10 min). (E) Live/dead assay in 3D multicellular HCT 116 spheroids under the same conditions listed for (D). (F) *Z*-stack images of eight 10-μm slices in the HCT 116 spheroids shown in (E).

considered to be the most significant tissue organs for the accumulation of albumin nanoparticles or AuNPs. As with the size of AuNCs/BSA-NPs, most nanoparticles of 20–150 nm are predominantly accumulated in the liver and spleen [19]. Our previous study also showed that albumin-associated gold nanoclusters (60–80 nm) was significantly accumulated in the liver [74]. In addition, nanoparticles of < 6 nm can be ultimately excreted to the urine through the glomerular filtration process [74,75]. Taken together, our AuNCs/BSA-NPs are predicted to be mainly accumulated in these organs as well as tumors, and the individual AuNPs detached from AuNCs or AuNCs/BSA-NPs would be cleared through the kidney.

Unlike the clearly visible xenografted tumors of mice, clinical tumors need to be visualized for further therapy. Targeted gold nanoparticles can be used to visualize tumors or other tissues using X-ray CT or PA imaging [29,30]. However, CT requires a large amount of gold nanoparticles, and PA imaging is suitable for local detection rather than

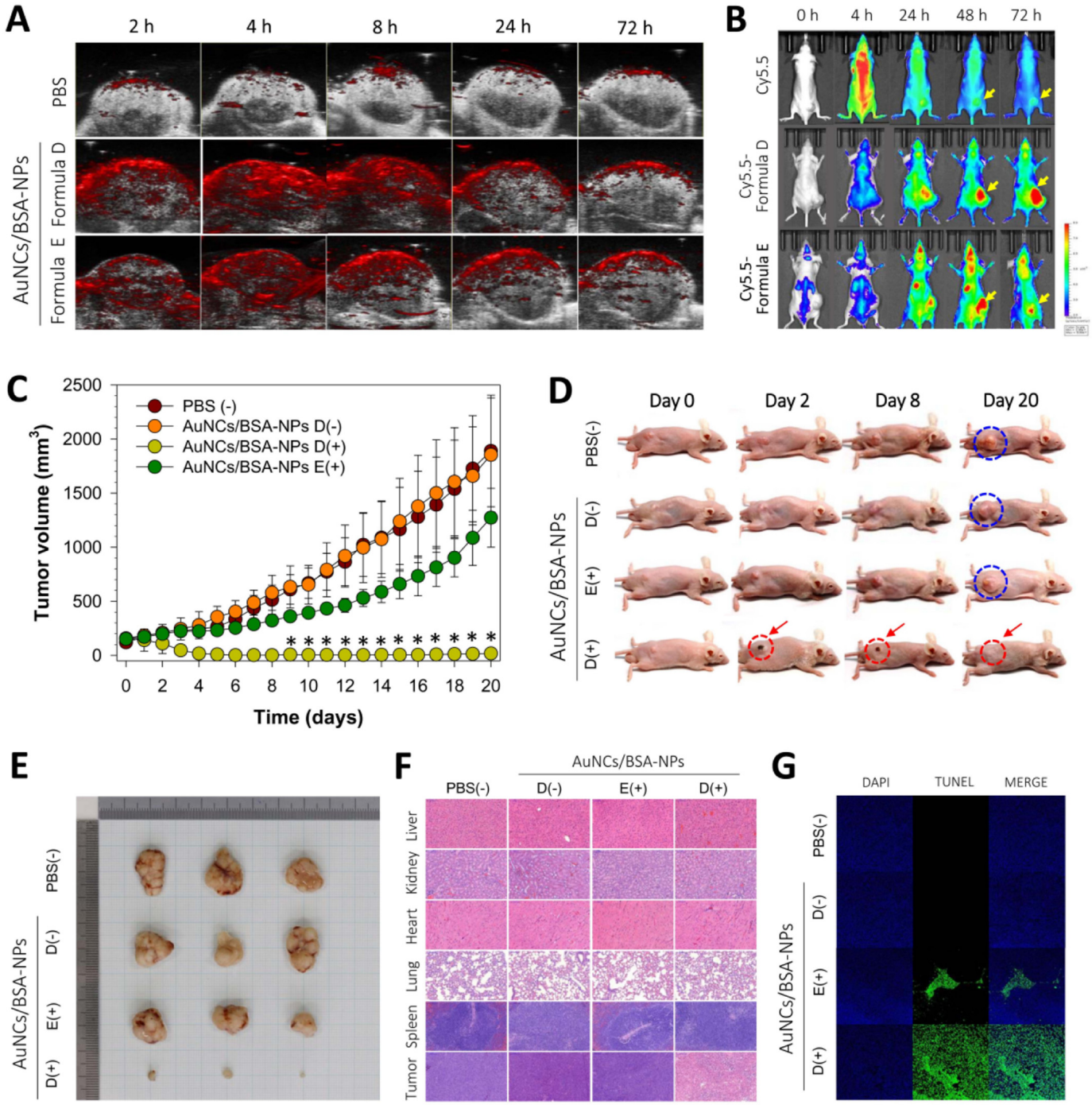

Fig. 6. (A) Photoacoustic imaging of PBS and AuNCs/BSA-NPs(D/E) at predetermined times after tail vein injection: dual-imaging of ultrasonic (white) and photoacoustic (red) regions. (B) *In vivo* optical imaging of PBS and AuNCs/Cy5.5-BSA-NPs(D/E) over 72 h. (C) Tumor growth curves of HCT116 tumor-bearing mice treated with PBS or AuNCs/BSA-NPs(D/E). (D) Photographs of HCT 116 tumor-bearing mice 20 days after photothermal therapy. (E) Size of excised tumors in each treatment group at day 20. (F) Histopathology of H&*E*-stained tumors and major tissue organs (liver, kidney, heart, lung, and spleen) after 20 days in each treatment group. (G) *In vivo* TUNEL assay to detect apoptosis in tumor tissues obtained from each group 24 h after laser irradiation. (For interpretation of the references to colour in this figure legend, the reader is referred to the web version of this article.)

whole-body detection. Magnetic resonance imaging (MRI) and positron emission tomography (PET) require additional magnetic probes or radioisotopes. In contrast, fluorescence-based optical imaging has the clear advantages of high sensitivity (10^{-12}) and good resolution (0.3 μm) [76]. However, as mentioned previously, hyperthermal AuNCs (> a few nanometers) lose fluorescence, unlike fluorescent AuNCs (< 1–2 nm), which undermines their use as fluorescence optical imaging agents [24–26]. To address this problem, we used albumin nanoparticles as second carriers to incorporate AuNCs and to allow for Cy5.5 attachment at a sufficient distance to prevent quenching by the AuNPs. Based on our assay results, the AuNCs/Cy5.5-BSA-NPs(D) described here appear to be suitable for optical imaging.

3.8. *In vivo* antitumor effect and histopathology induced by hyperthermia

Our final aim was to confirm the antitumor efficacy of AuNCs/BSA-

NPs(D). For this, tumor ablation induced by AuNCs/BSA-NPs(D/E) was investigated by monitoring tumor volumes in HCT116 tumor-bearing BALB/c nude mice. Photothermal treatment using AuNCs/BSA-NPs and 808 nm laser irradiation (1.5 W/cm^2, 10 min) was initiated when tumors reached a size of 150 mm^3 (on day 0). As shown in Fig. 6C, tumor growth in mice treated with AuNCs/BSA-NPs(D) plus 808 nm laser irradiation was remarkably suppressed, and tumor volume had decreased to 17.8 mm^3 on day 20 without tumor size rebound. In contrast, tumors of mice treated with either PBS without 808 nm laser or AuNCs/BSA-NPs(E) plus 808 nm laser were ~1850 and ~1250 mm^3, respectively (Fig. 6C–E). Additionally, the skin surface of tumors treated with AuNCs/BSA-NPs(D) plus the 808 nm laser was charred due to the strong hyperthermal effect of the AuNCs. Tumor nodules were no longer visible due to irreversible injury induced by high temperatures (> 50 °C) [57]. The body weights of mice in all groups remained stable without significant changes for over 20 days, indicating that all mice were well cared-for with no serious deleterious effects for the entire therapy period (data not shown).

The degree of tumor ablation induced by AuNCs/BSA-NPs was assessed from cell density and colour intensity measured in photos of H&*E*-stained tumor sections. As shown in Fig. 6F, tumor sections from mice treated with PBS without laser irradiation or with AuNCs/BSA-NPs(E) plus laser irradiation displayed typical overgrowth patterns with little damage, whereas tumor sections from mice treated with AuNCs/BSA-NPs(D) plus laser irradiation had a much lower density of cells and colors. H&E-stained sections of organs (liver, kidney, heart, lung, and spleen) did not reveal significant histological damage in any of the mouse groups, indicating that no significant toxicity had occurred. There was no histopathologic difference in major organs between the PBS-treated group and the AuNCs/BSA-NP-treated groups. The *in vivo* TUNEL assay was carried out 1 day after PPT. The nucleus of cells was stained blue with DAPI staining and fragmented DNA was stained green using FITC. Apoptotic cells have fragmented DNA and therefore fluoresce green [77]. TUNEL results showed that cells of tumors treated with AuNCs/BSA-NPs(D) and laser irradiation were killed, in part, by apoptosis as was well as necrosis due to burning (Fig. 6G).

4. Conclusions

In summary, we designed and fabricated heat- and fluorescence-emitting AuNC-loaded albumin nanoparticles (AuNCs/Cy5.5-BSA-NPs) by optimizing quantities of AuNPs/AuNCs and albumin based on consideration of interparticle distances. These hybrid AuNCs/BSA nanoparticles of ~150 nm displayed a good hyperthermal effect in response to NIR light (808 nm) and had well-preserved fluorescence intensity contributed by surface-modified Cy5.5. AuNCs/BSA-NPs remarkably suppressed the tumors of HCT116-bearing mice based on LSPR and allowed visualization of tumor sites due to a decrease in FRET. Together, these findings suggest that optimizing the interparticle distances between gold and carriers/probes is critical for producing gold nanoparticles that have a photothermal effect and can be used for optical imaging. Our gold nanocluster-incorporated albumin nanoparticles are a potential platform for treatment and diagnosis of colon cancers.

Acknowledgments

This research was supported by the Basic Science Research Program through the National Research Foundation of Korea (NRF) funded by the Ministry of Science and ICT (2017R1A2B2004955).

Appendix A. Supplementary data

Supplementary data to this article can be found online at https://doi.org/10.1016/j.jconrel.2019.04.036.

References

[1] W.I. Choi, J.-Y. Kim, C. Kang, C.C. Byeon, Y.H. Kim, G. Tae, Tumor regression in vivo by photothermal therapy based on gold-nanorod-loaded, functional nanocarriers, ACS Nano 5 (2011) 1995–2003.
[2] G. von Maltzahn, A. Centrone, J.H. Park, R. Ramanathan, M.J. Sailor, T.A. Hatton, S.N. Bhatia, SERS-coded gold nanorods as a multifunctional platform for densely multiplexed near-infrared imaging and photothermal heating, Adv. Mater. 21 (2009) 3175–3180.
[3] M. Converse, E.J. Bond, B. Veen, C. Hagness, A computational study of ultra-wideband versus narrowband microwave hyperthermia for breast cancer treatment, IEEE Trans. Microw. Theory Tech. 54 (2006) 2169–2180.
[4] R. Arthur, W. Straube, J. Trobaugh, E. Moros, Non-invasive estimation of hyperthermia temperatures with ultrasound, Int. J. Hyperth. 21 (2005) 589–600.
[5] X. Guo, J. You, Near infrared light-controlled therapeutic molecules release of nanocarriers in cancer therapy, J. Pharm. Investig. 47 (4) (2017) 297–316.
[6] N.S. Abadeer, C.J. Murphy, Recent progress in cancer thermal therapy using gold nanoparticles, J. Phys. Chem. C Nanomater. Interfaces 120 (2016) 4691–4716.
[7] A.M. Alkilany, L.B. Thompson, S.P. Boulos, P.N. Sisco, C.J. Murphy, Gold nanorods: their potential for photothermal therapeutics and drug delivery, tempered by the complexity of their biological interactions, Adv. Drug Deliv. Rev. 64 (2012) 190–199.
[8] H.S. Kim, D.Y. Lee, Photothermal therapy with gold nanoparticles as an anticancer medication, J. Pharm. Investig. 47 (1) (2017) 19–26.
[9] V.P. Zharov, K.E. Mercer, E.N. Galitovskaya, M.S. Smeltzer, Photothermal nanotherapeutics and nanodiagnostics for selective killing of bacteria targeted with gold nanoparticles, Biophys. J. 90 (2006) 619–627.
[10] D.V. Peralta, Z. Heidari, S. Dash, M.A. Tarr, Hybrid paclitaxel and gold nanorod-loaded human serum albumin nanoparticles for simultaneous chemotherapeutic and photothermal therapy on 4T1 breast cancer cells, ACS Appl. Mater. Interfaces 7 (2015) 7101–7111.
[11] K. Okajima, R.J. Griffin, K. Iwata, A. Shakil, C.W. Song, Tumor oxygenation after mild-temperature hyperthermia in combination with carbogen breathing: dependence on heat dose and tumor type, Radiat. Res. 149 (1998) 294–299.
[12] A. Shakil, J.L. Osborn, C.W. Song, Changes in oxygenation status and blood flow in a rat tumor model by mild temperature hyperthermia, Int. J. Radiat. Oncol. Biol. Phys. 43 (1999) 859–865.
[13] A.J. Gormley, N. Larson, A. Banisadr, R. Robinson, N. Frazier, A. Ray, H. Ghandehari, Plasmonic photothermal therapy increases the tumor mass penetration of HPMA copolymers, J. Control. Release 166 (2013) 130–138.
[14] P. Huang, J. Lin, W. Li, P. Rong, Z. Wang, S. Wang, X. Wang, X. Sun, M. Aronova, G. Niu, Biodegradable gold nanovesicles with an ultrastrong plasmonic coupling effect for photoacoustic imaging and photothermal therapy, Angew. Chem. Int. Ed. Engl. 125 (2013) 13958–13964.
[15] X. Huang, P.K. Jain, I.H. El-Sayed, M.A. El-Sayed, Plasmonic photothermal therapy (PPTT) using gold nanoparticles, Lasers Med. Sci. 23 (2008) 217–228.
[16] R. Weissleder, A clearer vision for in vivo imaging, Nat. Biotechnol. 19 (2001) 316–317.
[17] A.K. Murthy, R.J. Stover, A.U. Borwankar, G.D. Nie, S. Gourisankar, T.M. Truskett, K.V. Sokolov, K.P. Johnston, Equilibrium gold nanoclusters quenched with biodegradable polymers, ACS Nano 7 (2012) 239–251.
[18] J.M. Tam, J.O. Tam, A. Murthy, D.R. Ingram, L.L. Ma, K. Travis, K.P. Johnston, K.V. Sokolov, Controlled assembly of biodegradable plasmonic nanoclusters for near-infrared imaging and therapeutic applications, ACS Nano 4 (2010) 2178–2184.
[19] E. Blanco, H. Shen, M. Ferrari, Principles of nanoparticle design for overcoming biological barriers to drug delivery, Nat. Biotechnol. 33 (2015) 941–951.
[20] B. Du, X. Jiang, A. Das, Q. Zhou, M. Yu, R. Jin, J. Zheng, Glomerular barrier behaves as an atomically precise bandpass filter in a sub-nanometre regime, Nat. Nanotechnol. 12 (2017) 1096–1102.
[21] Y.H. Choi, H.-K. Han, Nanomedicines: current status and future perspectives in aspect of drug delivery and pharmacokinetics, J. Pharm. Investig. 48 (1) (2018) 43–60.
[22] H. Deng, F. Dai, G. Ma, X. Zhang, Theranostic gold nanomicelles made from biocompatible comb-like polymers for thermochemotherapy and multifunctional imaging with rapid clearance, Adv. Mater. 27 (2015) 3645–3653.
[23] H.S. Han, K.Y. Choi, H. Lee, M. Lee, J.Y. An, S. Shin, S. Kwon, D.S. Lee, J.H. Park, Gold-nanoclustered hyaluronan nano-assemblies for photothermally maneuvered photodynamic tumor ablation, ACS Nano 10 (2016) 10858–10868.
[24] J. Xie, Y. Zheng, J.Y. Ying, Protein-directed synthesis of highly fluorescent gold nanoclusters, J. Am. Chem. Soc. 131 (2009) 888–889.
[25] S. Shahsavari, F. Behroozi, Gold nanoclusters: nanomedicine potentials and applications, J. Nanomed. Res. 3 (2016) 00069.
[26] D. Punj, R. Regmi, A. Devilez, R. Plauchu, S.B. Moparthi, B. Stout, N. Bonod, H. Rigneault, J.r.m. Wenger, Self-assembled nanoparticle dimer antennas for plasmonic-enhanced single-molecule fluorescence detection at micromolar concentrations, ACS Photon. 2 (2015) 1099–1107.
[27] H. Hevekerl, T. Spielmann, A. Chmyrov, J. Widengren, Forster resonance energy transfer beyond 10 nm: exploiting the triplet state kinetics of organic fluorophores, J. Phys. Chem. B 115 (2011) 13360–13370.
[28] J. Li, F. Cheng, H. Huang, L. Li, J.-J. Zhu, Nanomaterial-based activatable imaging probes: from design to biological applications, Chem. Soc. Rev. 44 (2015) 7855–7880.
[29] W. Li, X. Chen, Gold nanoparticles for photoacoustic imaging, Nanomedicine 10 (2015) 299–320.

[30] D. Xi, S. Dong, X. Meng, Q. Lu, L. Meng, J. Ye, Gold nanoparticles as computerized tomography (CT) contrast agents, RSC Adv. 2 (2012) 12515–12524.
[31] J.H. Choi, Y.J. Lee, D. Kim, Image-guided nanomedicine for cancer, J. Pharm. Investig. 47 (1) (2017) 51–64.
[32] S. Bae, K. Ma, T.H. Kim, E.S. Lee, K.T. Oh, E.-S. Park, K.C. Lee, Y.S. Youn, Doxorubicin-loaded human serum albumin nanoparticles surface-modified with TNF-related apoptosis-inducing ligand and transferrin for targeting multiple tumor types, Biomaterials 33 (2012) 1536–1546.
[33] S.H. Choi, H.J. Byeon, J.S. Choi, L. Thao, I. Kim, E.S. Lee, B.S. Shin, K.C. Lee, Y.S. Youn, Inhalable self-assembled albumin nanoparticles for treating drug-resistant lung cancer, J. Control. Release 197 (2015) 199–207.
[34] H.J. Byeon, S. Lee, S.Y. Min, E.S. Lee, B.S. Shin, H.-G. Choi, Y.S. Youn, Doxorubicin-loaded nanoparticles consisted of cationic-and mannose-modified-albumins for dual-targeting in brain tumors, J. Control. Release 225 (2016) 301–313.
[35] W. Haiss, N.T.K. Thanh, J. Aveyard, D.G. Fernig, Determination of size and concentration of gold nanoparticles from UV-Vis spectra, Anal. Chem. 79 (2007) 4215–4221.
[36] P. Sanpui, A. Paul, A. Chattopadhyay, Theranostic potential of gold nanoparticle-protein agglomerates, Nanoscale 7 (2015) 18411–18423.
[37] Y. Xia, X. Wu, J. Zhao, J. Zhao, Z. Li, W. Ren, Y. Tian, A. Li, Z. Shen, A. Wu, Three dimensional plasmonic assemblies of AuNPs with an overall size of sub-200 nm for chemo-photothermal synergistic therapy of breast cancer, Nanoscale 8 (2016) 18682–18692.
[38] A. Jithan, K. Madhavi, M. Madhavi, K. Prabhakar, Preparation and characterization of albumin nanoparticles encapsulating curcumin intended for the treatment of breast cancer, Int. J. Pharm. Investig. 1 (2011) 119–125.
[39] M. Yu, J. Zheng, Clearance pathways and tumor targeting of imaging nanoparticles, ACS Nano 9 (2015) 6655–6674.
[40] A.A. Bhirde, S.A. Hassan, E. Harr, X. Chen, Role of albumin in the formation and stabilization of nanoparticle aggregates in serum studied by continuous photon correlation spectroscopy and multiscale computer simulations, J. Phys. Chem. C Nanomater. Interfaces 118 (2014) 16199–16208.
[41] B. Elsadek, F. Kratz, Impact of albumin on drug delivery—new applications on the horizon, J. Control. Release 157 (2012) 4–28.
[42] M.J. Hawkins, P. Soon-Shiong, N. Desai, Protein nanoparticles as drug carriers in clinical medicine, Adv. Drug Deliv. Rev. 60 (2008) 876–885.
[43] W. Lohcharoenkal, L. Wang, Y.C. Chen, Y. Rojanasakul, Protein nanoparticles as drug delivery carriers for cancer therapy, Biomed. Res. Int. 2014 (2014) 180549.
[44] F. Kratz, Albumin as a drug carrier: design of prodrugs, drug conjugates and nanoparticles, J. Control. Release 132 (2008) 171–183.
[45] Z. Liu, X. Chen, Simple bioconjugate chemistry serves great clinical advances: albumin as a versatile platform for diagnosis and precision therapy, Chem. Soc. Rev. 45 (2016) 1432–1456.
[46] S.Y. Min, H.J. Byeon, C. Lee, J. Seo, E.S. Lee, B.S. Shin, H.-G. Choi, K.C. Lee, Y.S. Youn, Facile one-pot formulation of TRAIL-embedded paclitaxel-bound albumin nanoparticles for the treatment of pancreatic cancer, Int. J. Pharm. 494 (2015) 506–515.
[47] E.N. Hoogenboezem, C.L. Duvall, Harnessing albumin as a carrier for cancer therapies, Adv. Drug Deliv. Rev. 130 (2018) 73–89.
[48] S. Nitta, K. Numata, Biopolymer-based nanoparticles for drug/gene delivery and tissue engineering, Int. J. Mol. Sci. 14 (2013) 1629–1654.
[49] C. Lee, B. Kim, S. Lee, T.H. Kim, J.O. Kim, E.S. Lee, K.T. Oh, H.-G. Choi, S.D. Yoo, Y.S. Youn, Doxorubicin and paclitaxel co-bound lactosylated albumin nanoparticles having targetability to hepatocellular carcinoma, Colloids Surf. B 152 (2017) 183–191.
[50] E.S. Lee, Y.S. Youn, Albumin-based potential drugs: focus on half-life extension and nanoparticle preparation, J. Pharm. Investig. 46 (2016) 305–315.
[51] A.O. Elzoghby, W.M. Samy, N.A. Elgindy, Albumin-based nanoparticles as potential controlled release drug delivery systems, J. Control. Release 157 (2012) 168–182.
[52] K. Langer, S. Balthasar, V. Vogel, N. Dinauer, H. Von Briesen, D. Schubert, Optimization of the preparation process for human serum albumin (HSA) nanoparticles, Int. J. Pharm. 257 (2003) 169–180.
[53] C. Weber, C. Coester, J. Kreuter, K. Langer, Desolvation process and surface characterisation of protein nanoparticles, Int. J. Pharm. 194 (2000) 91–102.
[54] S.M. Ahsan, C.M. Rao, The role of surface charge in the desolvation process of gelatin: implications in nanoparticle synthesis and modulation of drug release, Int. J. Nanomedicine 12 (2017) 795–808.
[55] C. Lee, H.S. Hwang, S. Lee, B. Kim, J.O. Kim, K.T. Oh, E.S. Lee, H.G. Choi, Y.S. Youn, Rabies virus-inspired silica-coated gold nanorods as a photothermal therapeutic platform for treating brain tumors, Adv. Mater. 29 (2017) 1605563.
[56] L.A. Sordillo, Y. Pu, S. Pratavieira, Y. Budansky, R.R. Alfano, Deep optical imaging of tissue using the second and third near-infrared spectral windows, J. Biomed. Opt. 19 (2014) 056004.
[57] D. Jaque, L. Martinez Maestro, B. del Rosal, P. Haro-Gonzalez, A. Benayas, J.L. Plaza, E. Martin Rodriguez, J. Garcia Sole, Nanoparticles for photothermal therapies, Nanoscale 6 (2014) 9494–9530.
[58] R. Elghanian, J.J. Storhoff, R.C. Mucic, R.L. Letsinger, C.A. Mirkin, Selective colorimetric detection of polynucleotides based on the distance-dependent optical properties of gold nanoparticles, Science 277 (1997) 1078–1081.
[59] P.K. Jain, M.A. El-Sayed, Plasmonic coupling in noble metal nanostructures, Chem. Phys. Lett. 487 (2010) 153–164.
[60] K.-H. Su, Q.-H. Wei, X. Zhang, J. Mock, D.R. Smith, S. Schultz, Interparticle coupling effects on plasmon resonances of nanogold particles, Nano Lett. 3 (2003) 1087–1090.
[61] W.C. Zhang, Q. Li, M. Qiu, A plasmon ruler based on nanoscale photothermal effect, Opt. Express 21 (2013) 172–181.
[62] J. Qiu, W.D. Wei, Surface plasmon-mediated photothermal chemistry, J. Phys. Chem. C Nanomater. Interfaces 118 (2014) 20735–20749.
[63] S. Li, T. Zhang, Z. Zhu, N. Gao, Q.-H. Xu, Lighting up the gold nanoparticles quenched fluorescence by silver nanoparticles: a separation distance study, RSC Adv. 6 (2016) 58566–58572.
[64] M. Swierczewska, S. Lee, X. Chen, The design and application of fluorophore-gold nanoparticle activatable probes, Phys. Chem. Chem. Phys. 13 (2011) 9929–9941.
[65] E. Dulkeith, M. Ringler, T.A. Klar, J. Feldmann, A.M. Javier, W.J. Parak, Gold nanoparticles quench fluorescence by phase induced radiative rate suppression, Nano Lett. 5 (2005) 585–589.
[66] A. Polemi, K.L. Shuford, Distance dependent quenching effect in nanoparticle dimers, J. Chem. Phys. 136 (2012) 184703.
[67] G.P. Acuna, M. Bucher, I.H. Stein, C. Steinhauer, A. Kuzyk, P. Holzmeister, R. Schreiber, A. Moroz, F.D. Stefani, T. Liedl, F.C. Simmel, P. Tinnefeld, Distance dependence of single-fluorophore quenching by gold nanoparticles studied on DNA origami, ACS Nano 6 (2012) 3189–3195.
[68] R.A. Petros, J.M. DeSimone, Strategies in the design of nanoparticles for therapeutic applications, Nat. Rev. Drug Discov. 9 (2010) 615–627.
[69] P.T.T. Phuong, S. Lee, C. Lee, B. Seo, S. Park, K.T. Oh, E.S. Lee, H.-G. Choi, B.S. Shin, Y.S. Youn, Beta-carotene-bound albumin nanoparticles modified with chlorin e6 for breast tumor ablation based on photodynamic therapy, Colloids Surf. B 171 (2018) 123–133.
[70] B. Storp, A. Engel, A. Boeker, M. Ploeger, K. Langer, Albumin nanoparticles with predictable size by desolvation procedure, J. Microencapsul. 29 (2012) 138–146.
[71] Y. Sun, H. Jiang, B.E. O'Neill, Photoacoustic imaging: An emerging optical modality in diagnostic and theranostic medicine, J. Biosens. Bioelectron. 2 (2011) 1000108.
[72] W.W. Li, X.Y. Chen, Gold nanoparticles for photoacoustic imaging, Nanomedicine (Lond) 10 (2015) 299–320.
[73] A. Hahnenkamp, W. Alsibai, C. Bremer, C. Holtke, Optimizing the bioavailability of small molecular optical imaging probes by conjugation to an albumin affinity tag, J. Control. Release 186 (2014) 32–40.
[74] S. Lee, C. Lee, S. Park, K. Lim, S.S. Kim, J.O. Kim, E.S. Lee, K.T. Oh, H.-G. Choi, Y.S. Youn, Facile fabrication of highly photothermal-effective albumin-assisted gold nanoclusters for treating breast cancer, Int. J. Pharm. 553 (1–2) (2018) 363–374.
[75] J. Liu, M. Yu, C. Zhou, J. Zheng, Renal clearable inorganic nanoparticles: a new frontier of bionanotechnology, Mater. Today 16 (12) (2013) 477–486.
[76] J. Key, J.F. Leary, Nanoparticles for multimodal in vivo imaging in nanomedicine, Int. J. Nanomedicine 9 (2014) 711–726.
[77] Z. Darzynkiewicz, D. Galkowski, H. Zhao, Analysis of apoptosis by cytometry using TUNEL assay, Methods 44 (2008) 250–254.